Chromatin and Cytoskeletal Tethering Determine Nuclear Morphology in Progerin-Expressing Cells

Maria Chiara Lionetti,[1] Silvia Bonfanti,[2] Maria Rita Fumagalli,[1,3] Zoe Budrikis,[2] Francesc Font-Clos,[2] Giulio Costantini,[2] Oleksandr Chepizhko,[4] Stefano Zapperi,[2,5] and Caterina A. M. La Porta[1,3,*]

[1]Center for Complexity and Biosystems, Department of Environmental Science and Policy and [2]Center for Complexity and Biosystems, Department of Physics, University of Milan, Milano, Italy; [3]CNR-Consiglio Nazionale delle Ricerche, Biophysics institute, Genova, Italy; [4]Institut für Theoretische Physik, Leopold-Franzens-Universität Innsbruck, Innsbruck, Austria; and [5]CNR-Consiglio Nazionale delle Ricerche, Istituto di Chimica della Materia Condensata e di Tecnologie per l'Energia, Milano, Italy

ABSTRACT The nuclear morphology of eukaryotic cells is determined by the interplay between the lamina forming the nuclear skeleton, the chromatin inside the nucleus, and the coupling with the cytoskeleton. Nuclear alterations are often associated with pathological conditions as in Hutchinson-Gilford progeria syndrome, in which a mutation in the lamin A gene yields an altered form of the protein, named progerin, and an aberrant nuclear shape. Here, we introduce an inducible cellular model of Hutchinson-Gilford progeria syndrome in HeLa cells in which increased progerin expression leads to alterations in the coupling of the lamin shell with cytoskeletal or chromatin tethers as well as with polycomb group proteins. Furthermore, our experiments show that progerin expression leads to enhanced nuclear shape fluctuations in response to cytoskeletal activity. To interpret the experimental results, we introduce a computational model of the cell nucleus that explicitly includes chromatin fibers, the nuclear shell, and coupling with the cytoskeleton. The model allows us to investigate how the geometrical organization of the chromatin-lamin tether affects nuclear morphology and shape fluctuations. In sum, our findings highlight the crucial role played by lamin-chromatin and lamin-cytoskeletal alterations in determining nuclear shape morphology and in affecting cellular functions and gene regulation.

SIGNIFICANCE Hutchinson-Gilford progeria syndrome is a rare disease characterized by accelerated aging due to a mutation of the lamin A gene, leading to an aberrant protein—named progerin—and to the formation of nuclear blebs. We combine experiments on a cellular model reproducing Hutchinson-Gilford progeria syndrome cells and numerical simulations of nuclear mechanics to study the biological and biophysical effects of progerin expression on nuclear morphology and functioning. Our results show that progerin induces key changes in the mechanical tethering between cytoskeleton, lamins, and chromatin, producing nuclear shape alterations and affecting gene regulation.

INTRODUCTION

The cell nucleus is of crucial importance in eukaryotic cells because it harbors and preserves the genetic information encoded into chromatin fibers. The protective role of the nucleus is ensured by its structural and mechanical features, mainly because of a rigid nuclear shell composed by a dense network of filaments assembled from lamin proteins. The relative concentration of the different types of lamins (e.g., lamin A, B, and C) composing the nuclear skeleton can have an important effect on the elastic and viscoelastic response of the nucleus (1,2), affecting gene expression and

cell fate, too (3). There is increasing awareness that the mechanical properties of the nucleus are not only determined by the properties of the nuclear skeleton but crucially depend on the tethering between chromatin and lamins (4) and on the coupling between lamins and cytoskeleton (5,6). In particular, lamin A is involved in a complex molecular interface between the inner membrane of the nuclear envelope and chromatin fibers (7), and the integrity of this interface is crucial for correct chromatin functioning during cell cycle and apoptosis. Lamin mutations can thus lead to severe morphological and mechanical nuclear alterations, often associated with severe pathological conditions (8). For instance, Hutchinson-Gilford progeria syndrome (HGPS) is a rare autosomal-dominant disease characterized by accelerated aging due to a de novo mutation in the LMNA gene, leading to an aberrant form of the protein

known as progerin (9). Cells from HGPS patients typically display altered nuclear shapes with bleb-like protrusions.

Although the genetic origin of HGPS has been clarified (9), the precise mechanism leading to the changes in nuclear morphology is still unknown. In addition to blebs, nuclei from HGPS patients also display gross reorganization of the lamin architecture into distinct domains (10) and mechanical stiffness alterations (10,11). Recent experiments using micropipette aspiration show that nuclei expressing exogenous progerin are also stiffer with respect to control cells (12), resembling the HGPS phenotype (10). These works also found that inside the nucleus, chromatin is softer and displays reduced mobility when progerin is expressed (12). Interestingly, progerin expression is found to reduce the extent of mechanical force propagation to the nuclear interior from the cytoskeleton (12).

The mechanical coupling between the cytoskeleton, nuclear envelope, and chromatin fibers is mediated by a set of key proteins acting as connectors between the different elements. In particular, Sun proteins, located in the inner nuclear membrane, are known to interact with lamins in the nucleoplasm, whereas nesprin (KASH) recruits cytoskeletal components to the outer nuclear membrane. Sun proteins also interact with the protein emerin (13), which is located in the inner nuclear membrane and is directly linked to lamin A (14). Emerin is known to act as a chromatin tether, and its mutation may cause Emery-Dreifuss muscular dystrophy. It is interesting to note that Emery-Dreifuss muscular dystrophy may also display mutations in nesprin-1 and 2 (15) and SUN1 (16), leading to a softer nucleus and looser association with lamin A (17). Another key protein for nuclear mechanics is fascin, a F-actin-binding protein (18) that plays a role in the stabilization of filopodia (19) and in the molecular adhesion dynamics of migrating cells (20). A recent study shows that fascin can bind directly to nesprin-2 at the nuclear envelope, and this interaction is independent of the role of fascin within filopodia at the cell periphery (21). Moreover, it has been shown that the disruption of this interaction induces important changes in nuclear shape and deformation (21). In particular, uncoupling the S39-phospho-fascin/nesprin-2 complex leads to a reduction of nuclear deformation and affects, in a significant way, many functional properties such as cell invasion (21).

Several computational models have been used to investigate nuclear mechanics, treating the nuclear skeleton either as a discretized continuous elastic shell (22,23) or as a polymer network (24,25). Numerical simulations of a finite element model for the nuclear skeleton reveal that blebs are formed under the assumption that the shell is characterized by domains with different relative concentrations of lamin A and B (23). According to this model, blebs would form in correspondence with domains that are rich in lamin A, which would make them prone to expansion (23). The model provides a good description of the morphology of

the nuclei of lamin B-silenced cells, but its application to HGPS cells is not straightforward. Lamin domains have been observed in HGPS nuclei thanks to polarized light microscopy showing regions with distinct orientations in the lamin network (10). Different lamin domains in HGPS nuclei thus mostly differ because of their orientation rather than because of their relative lamin content, contrary to the model hypothesis (23). The model did not consider the coupling between lamins and chromatin that is known to be important for nuclear morphology and mechanics (4,26,27).

In this work, we investigated experimentally and computationally the role of chromatin and cytoskeletal tethering in affecting nuclear morphology and function in progerin-expressing cells. To tackle this question, we introduced an in vitro cellular model in which progerin expression was induced at controlled and realistic levels in HeLa cells, thanks to the Tet-On technology. Our model was useful to overcome the limitations posed by the use of human fibroblasts obtained from HGPS patients that are only able to grow in vitro for a few passages. We used our cellular model to investigate how the induction of progerin expression affects key proteins involved in the coupling of the nuclear shell with the cytoskeleton and with chromatin fibers. We then studied how alterations of these couplings impacted on critical nuclear functions and could possibly lead to changes in gene regulation.

To interpret the experimental results, we constructed a mechanical model of the cell nucleus that included the coupling between nuclear lamina, chromatin fibers, and the cytoskeleton. To model chromatin fibers, we followed previous polymer models (28,29) that have been successfully used to study chromatin organization in the nucleus (30,31). Chromatin fibers were tethered to a lamin shell, modeled by a triangulated surface endowed with stretching and bending rigidity, that is also elastically tethered to an external set of oscillating points modeling contractions of the cytoskeleton. The computational model allowed us to test in silico the effect of tether organization and strength on nuclear morphology and explain the presence of enhanced cytoskeleton-induced nuclear fluctuations that we observed experimentally when progerin expression was induced. Altogether, our findings highlight the important role played by chromatin and nuclear tethering in determining nuclear morphology and fluctuations with important implications for HGPS.

MATERIALS AND METHODS

Human fibroblast culture growth conditions

Human fibroblasts from an HGPS patient (HGSDNF167) and the healthy mother of this patient (HGMDF090) were obtained from The Progeria Foundation Cell and Tissue Bank. The HGPS patient was a male of 8 years old with the classical mutation (heterozygous LMNA Exon 11 c1824 $C > T$ (p.Gly608Gly)). The cells were maintained according to the protocol

reported by The Progeria Foundation: 15% fetal bovine serum (FBS), Dulbecco's modified Eagle's medium (DMEM) with 1% antibiotics, and 1% L-glutamine. The cells were detached by trypsin 0.25% EDTA and are maintained in culture for no more than five passages.

Plasmids and subcloning

Δ50-lamin A plasmid was obtained from Addgene (pEGFP-D50 lamin A, cod. 17653; Cambridge, MA). Plasmid expressing pTRE3G-mCherry vector was obtained from Clontech (cod. 631165; Mountain View, CA). *Escherichia coli* One Shot TOP10 bacteria (C404006; Invitrogen, Carlsbad, CA) were used for transformation with pEGFP-Δ50 lamin A and pTRE3G-mCherry vector. Competent cells were expanded and selected in Luria Broth medium (12795-027; Invitrogen) containing kanamycin for pEGFP Δ50-lamin A (K13747; Sigma-Aldrich, St. Louis, MO) and 100 μg/mL ampicillin (A5354; Sigma-Aldrich) for pTRE3G-mCherry vector for 18 h at 37°C. An AfeI/BamHI fragment containing the coding reading sequence of Δ50 lamin A was excised by a pEGFP-Δ50 lamin A plasmid (AfeI, cod. R0652S; New England Biolabs, Ipswich, MA) and subcloned into pTRE3G-mCherry vector linearized with EcorV (cod. R1095S; New England Biolabs) and BamHI (cod. R0136S; New England Biolabs) restriction enzymes according to the manufacturer's instructions. DNA fragments and vectors were routinely analyzed by electrophoresis on 1% agarose gel in 1× TAE (GellyPhor EMR010100; Euroclone, Milan, Italy). To recover DNA-digested fragments and linearized vectors after electrophoresis and proceed with subcloning, low-melting GellyPhor was used (cod. EMR911100; Euroclone). Promega T4 DNA ligase (cod. M1801; Promega, Madison, WI) was used to allow a ligation step according to the manufacturer's protocols. DNA fragments and vectors were routinely analyzed by electrophoresis on 1% agarose gel (GellyPhor, cod. EMR010100; Euroclone) in 1× TAE, whereas low-melting agarose gel (Gellyphor, cod. EMR911100; Euroclone) was used for the recovery of DNA fragments after electrophoresis. To purify DNA fragments from agarose gels, a QIAquick Gel Extraction Kit (Qiagen, Hilden, Germany) was used according to the manufacturer's instructions. To recover DNA-digested fragments and linearized vectors after electrophoresis and proceed with subcloning, Promega T4 DNA ligase (cod. M1801; Promega) was used to allow a ligation step according to the manufacturer's protocols. Promega PureYield Plasmid Miniprep and Midiprep (cod. A1330 and A2492; Promega) were used to purify plasmidic DNA. The product of this subcloning strategy was sequenced (Eurofins Genomics Service, Luxembourg, Luxembourg) using IRES and SV40 primers (IRES2_F: 5′-TGTGGAAAGAGTCAAATGGCT-3′, SV40_R: 5′-CTGCTCCCATT CATCAGTTCC-3′) to confirm that Δ50-lamin A was cloned in frame with the start codon at the IRES2/MCS junction (see Table S1).

Progerin inducible Tet-On HeLa cells

HeLa 3G cells (cod. 631183; Clontech) were cultured in DMEM (cod. ECB7501L; Euroclone) supplemented with 10% v/v Tet-free FBS (cod. ECS01821; Euroclone), 1% penicillin/streptomycin, and 1% L-glutamine at 37°C and 5% CO_2 in a humidified incubator immediately upon thawing without selective resistance. To create a double-stable inducible HeLa 3G cell line expressing Δ50 lamin A, HeLa 3G cells were transfected with 5 μg of pTRE3G-mCherry-Δ50-lamin A using Xfect reagent (cod. 631317; Clontech) and 250 ng of puromycin linear selection marker (cod. 631626; Clontech) according to the manufacturer's instructions to generate a double-stable cell line expressing both Tet-On 3G transactivator and higher levels of progerin in response to doxycycline (Doxy). After 2 weeks of drug selection, 24 resistant colonies were picked up and screened for inducibility, with increasing doses of Doxy (0, 1, 5, 10, and 20 ng/mL) measuring mCherry and Δ50 lamin A by immunofluorescence and Western blot. Two clones of the 24 screened were selected and used for further experiments. 48 h post-transfection, the cells were split into 4 × 10 cm dishes,

and 0.5 μg/mL of puromycin (cod. A11138-03; Life Technologies) and 200 μg/mL G418 (cod. A1720; Sigma-Aldrich) was added to select the positive clones. Drug-resistant colonies appeared 2 weeks after selection. Single clones were isolated using cloning cylinder (catalog cod. C1059; Sigma-Aldrich). When they reached confluence, the cells were split into six-well plate for testing the expression of Δ50 lamin A and for further maintenance. To express Δ50 lamin A in a dose-dependent manner, the cells were induced with Doxy (cod. 631311; Clontech) at the concentration indicated in the figures and analyzed 48 h after the induction. HeLa 3G cells expressing Δ50 lamin A were routinely maintained in culture in DMEM (cod. ECB7501L; Euroclone) supplemented with 10% v/v Tet-free FBS (cod. ECS01821; Euroclone), 200 μ/mL G418, and 0.25 μg/mL puromycin, 1% penicillin/streptomycin, and 1% L-glutamine at 37°C and 5% CO_2.

Δ50 lamin A and wild-type lamin A transient transfection

Plasmid containing the human lamin A-C-18 (cod. 55068; Addgene) or progerin (pEGFP-Δ50 lamin A, cod. 17653; Addgene) were purchased by Addgene. *E. coli* One Shot TOP10 bacteria (cod. C404006; Invitrogen) were transformed with plasmids, expanded, and selected in Luria Broth medium (cod. 12795-027; Invitrogen) containing 50 μg/mL kanamycin. PureYield Plasmid Miniprep and Midiprep (cod. A1330 and A2492; Promega) were used to purify plasmidic DNA according to the manufacturer's instructions.

HeLa cells were maintained in DMEM (cod. ECM0060L; Euroclone) medium with 10% FBS (ECS0180L; Euroclone), 100 U/mL penicillin, 100 mg/mL streptomycin sulfate (cod. ECB3001D; Euroclone), and 2 mM L-glutamine (cod. ECB3000D-20; Euroclone) at 37°C in an atmosphere of 5% CO2 and 95% humidity. Cells seeded at a 70% confluent onto six-well plates were transiently transfected with pEGFP Δ50 lamin A (cod. 17653; Addgene) or mEmerald-wild-type (WT)-lamin A (cod. 54139; Addgene) using Xfect transfection reagent (cod. 631317; Clontech). After 48 h from transfection, cells were used for the cytoskeleton pharmacological perturbation experiment.

Pharmacological perturbation of the cytoskeleton

To study the role of cytoskeleton in this context, actin and myosin organization were perturbed by exposing pEGFP-Δ50 lamin A or mEmerald-WT-lamin A overexpressing cells to blebbistatin, a myosin inhibitor, or to a cell-permeable inhibitor of formin-mediated actin nucleation and formin-mediated elongation of actin filaments, SMIFH2 (5). Subconfluent HeLa cells expressing WT or Δ50 lamin A were exposed to 25 μM blebbistatin (B0560; Sigma-Aldrich) for 30 min or to 20 μM SMIFH2 (S4826; Sigma-Aldrich) for 1 h at 37°C and 5% CO_2 in a humidified incubator. 5 min before the end of the treatment, Hoechst (1:1000, H3570; Life Technologies, Carlsbad, CA) was added to the cell medium to counterstain nuclei. Immediately after the end of each treatment, medium containing drugs was replaced with fresh medium, and cells were time-lapse imaged (one shot every 15 min) for 1 h using a Leica TCS NT confocal microscope (63×; Wetzlar, Germany) with a z-stack of 0.5 μm.

Immunofluorescence

Subconfluent cells grown on glass coverslips were fixed with 3.7% paraformaldehyde in phosphate-buffered saline (PBS) for 10 min or with ice-cold 100% methanol for 5 min at −20°C, permeabilized with 0.5% Triton X-100 in PBS for 5 min at room temperature (RT), and incubated with 10% goat serum in PBS for 1 h. The cells were stained with anti-lamin A (1:100 ab8980; Abcam, Cambridge, UK) or anti-PanLamin (1:50, ab20740; Abcam) or anti-progerin (1:20, ab66587; Abcam) or HP1 (1:250, ab109028; Abcam) overnight at 4°C. Thus, after a brief washing with PBS, the cells were incubated with the secondary antibody (1:250, anti-rabbit, ab150077; Abcam or anti-mouse, ab150113; Abcam) for 1 h. The nuclei

were counterstained with DAPI, and the slides were mounted with Pro-long antifade reagent (cod. P36931; Life Technologies). The images were acquired with a Leica TCS NT confocal microscope. Immunofluorescence intensity was estimated using a customized ImageJ macro evaluating single pixel fluorescence after subtracting the background noise. The average fluorescence was calculated on pixels that passed the background filtering. In all the analyzed frames, nuclei close to the edge of the image or superimposed were manually discarded.

Proximity ligation assay

Subconfluent cells were fixed on slides with ice-cold 100% methanol for 5 min at $-20°C$ and then incubated with Duolink Blocking Solution for 60 min at $37°C$ in a humidity chamber. Slides were then incubated in a humidity chamber overnight at $4°C$ with lamin A (1:100, cod. ab8980; Abcam) or PanLamin (1:50, cod. ab20740; Abcam) antibody with SUZ12 (1:800, mAb 3737; Cell Signaling Technology, Danvers, MA) or BMI1 (1:600, mAb6964; Cell Signaling Technology) or SUN1 (1:200, ab103021; Abcam) or emerin (1:200, ab40688; Abcam). After washing, samples were incubated in a preheated humidity chamber for 1 h at $37°C$ with anti-rabbit PLUS and anti-mouse MINUS PLA probes diluted 1:5. PLA probes generate a fluorescent signal when bound to two different primary antibodies, raised in different species, that recognize two antigens in close proximity (less than 40 nm). All the antibodies were diluted in Duolink Antibody Diluent. Ligation and amplification steps were performed according to manufacturer's instructions. Slides were mounted with Duolink In Situ Mounting Medium with DAPI (DUO82040; Sigma-Aldrich). The images were acquired with a Leica TCS NT confocal microscope.

Proximity ligation assay analysis

Immunofluorescence images were analyzed using existing and customized plugins of the bioimage informatics platform Icy (v.1.9.4 and 1.9.5 (32)) and custom python scripts. Reconstruction of the progerin Tet-On HeLa nuclear envelope was performed on all the Z-stacks with Icy HK-Means and ActiveContour plugin using the DAPI signal, and the resulting three-dimensional (3D) meshes were exported as VTK files. A wide range of parameters was explored to ensure that our results were not affected by the specific parameters chosen for reconstruction. Duolink spot recognition was performed separately on each nucleus with a semiautomatic protocol involving HK-means thresholding (ICY Thresholder plugin). The minimal size of each accepted spot was set to 70 pixels. Center of mass was used to determine the relative position of the spot respect to the nuclear envelope, and spots inside reconstructed nuclear mesh were taken into account. In all the analyzed frames, nuclei close to the borders or superimposed were manually discarded.

Immunoprecipitation assay

Subconfluent cells were gently detached from the culture plates using a cell lifter in cold PBS, collected in a 1.5 mL Eppendorf tube, and centrifuged at $3.5 \times 10^3 \times g$ for 5 min at $4°C$. The pellet was resuspended in lysis buffer (2 mM EGTA, 0.5 mM EDTA, 0.5 mM PMSF, $1\times$ TRITONX100, $1\times$ Protease Cocktail, P8340; Sigma-Aldrich) and incubated on ice for 30 min with periodic mix by vortex. The lysate was centrifuged at $14 \times 10^3 \times g$ for 10 min at $4°C$, the supernatant transferred to a fresh tube, and protein concentration was measured by DC Protein Assay Kit (Bio-Rad, Hercules, CA). 500 μg of total proteins was incubated with anti-fascin antibody (1:100, ab126772; AbCam) overnight at $4°C$ under stirring. 50% bead slurry of Protein A-Agarose (P9269; Sigma-Aldrich) was added to the lysate and reincubated with gentle rocking for 2 h at $4°C$ before centrifugation ($14 \times 10^3 \times g$ for 10 min at $4°C$). After three washes with 500 μL of lysis buffer, the sample was resuspended in 30 μL $2\times$ Laemmli sample buffer (2% SDS, 20% glycerol, and 125 mM Tris-HCl (pH 6.8)). Samples

were then heated to $90°C$ for 5 min, and 15 μL per sample was loaded on 10% SDS-PAGE for Western blot. 50 μg of the whole lysate for each sample was loaded on the same gel.

Western blot

Subconfluent cells were lysed by boiling in a modified Laemmli sample buffer (2% SDS, 20% glycerol, and 125 mM Tris-HCl (pH6.8)). The protein concentration was measured by DC Protein Assay Kit (Bio-Rad). Equal amounts of proteins were loaded on a 10% (or 7.5% for IP assay) SDS-PAGE gel and transferred to a PVDF membrane (Trans-Blot Turbo Mini PVDF; Bio-Rad). After blocking with 5% bovine serum albumin/0.1% Tween20 in PBS for 1 h at RT, the sheet was incubated with primary antibody overnight at $4°C$. The following antibodies and dilution were used in various experiments: anti-nesprin 2 (1:1000, cod. MABC86; Merck Millipore, Burlington, MA), anti-SUN1 (1:1000, ab103021; Abcam), anti-emerin (1:200 ab40688; Abcam), anti-S39-phospho-fascin antibody (1:10,000, ab90648; AbCam), anti-fascin (1:10,000, ab126772; AbCam), anti-SUZ12 (1:1000, cod. 3737; Cell Signaling Technology), anti-Ezh2 (1:1000, cod. 5246; Cell Signaling Technology), anti-Ring1A (1:1000, cod. 13069; Cell Signaling Technology), anti-RING1B (1:1000, cod. 5694; Cell Signaling Technology), anti-BMI1 (1:1000, cod. 6964; Cell Signaling Technology), anti-vinculin (1:10,000, cod. V9264; Sigma-Aldrich), anti-GAPDH (1:5000, cod. G9545; Sigma-Aldrich), or anti-β-tubulin (1:5000, cod. T8328; Sigma-Aldrich) antibodies incubated for 1 h at RT were used as housekeeping reference.

Wound-healing assay

For the migration assay, a wound is introduced in the central area of the confluent cell sheet by using a pipette tip, and the migration is followed by time-lapse imaging. The measurements of the velocity field were done using the PIVlab app for MATLAB (The MathWorks, Natick, MA) (33). The method is based on the comparison of the intensity fields of two consequent photographs of cells. The difference in the intensity is converted into velocity field measured in pixel/frames and then converted to $\mu m/h$ (34). The front position is quantified according to (34).

2D analysis of nuclear morphology

Nuclear segmentation

The transformation of fluorescence images into binary masks is done using a custom script in MATLAB. Using a two-peak histogram of pixel intensity, a threshold is defined for each image to cut away the background with uneven illumination. After applying this threshold, the "imbinarize" function is used with adaptive thresholding. Holes in the image are filled with the "imfill" function. The little remaining noise is removed with the "bwareaopen" function. The functions are a part of the MATLAB Image Processing Toolbox. We process 96 fluorescence images automatically and then manually check for segmentation errors. Usually, cells that are undergoing division or cells in regions of lower fluorescence intensity are not well segmented by our algorithm. After discarding segmentation errors by hand, we are left with binary masks of 297 No Doxy nuclei, 330 Doxy nuclei, 87 healthy nuclei, and 87 HGPS nuclei.

Computation of local curvature

The curvature of a point in a planar curve (x, y) is mathematically defined as

$$k = \frac{x'y'' - y'x''}{\left(x'^2 + y'^2\right)^{3/2}} \quad (1)$$

and corresponds to the inverse of the radius of a circle tangent to the point. To estimate the curvature of nuclei along each point of their perimeter, we

first fit fourth-order splines to the border of the binary masks using the "UnivariateSpline" function from SciPy python library (35), then evaluate Eq. 1 using the obtained differentiable curves.

Blebbiness index

Negative curvature in two-dimensional images is a signal of abnormal nuclear morphology, being associated with blebs and invaginations. Curvature changes along the perimeter of a nucleus, making it difficult to compare curvature estimates among large number of nuclei. To simplify the curvature values of nuclei along their perimeters into a single number for each nucleus, we define the blebbiness index ϕ as the weighted fraction of negative curvature,

$$\phi = \frac{\int_{\mathscr{C}_-} |k|}{\int_{\mathscr{C}} 1}, \tag{2}$$

where C is the perimeter of the nucleus and C_- is the region of the perimeter with negative curvature $k < 0$. The denominator $\int_{\mathscr{C}} 1$ is simply the length of the perimeter, and the numerator is the integral of the absolute value of the curvature along regions of negative curvature. In this way, regions of large negative curvature contribute more to the total than regions of negative but small curvature, making in turn the index ϕ robust to variability in the estimation of k.

Automated bleb counting

Automated bleb counting is a difficult problem. Although the biological definition of bleb is well established, a translation into quantitative terms admits different formulations. Here, we estimate the number of blebs by counting the number of regions of negative local curvature k along the nuclei perimeter. To avoid spurious results due to values of $k \simeq 0$, we define the number of blebs as the number of regions where the curvature is below a threshold $k_{\min} = -0.1$. Notice that we have a total of $N = 801$ nuclei, making manual quantification unfeasible in this case.

3D analysis of nuclear morphology

Mesh reconstruction of the nuclear shell

The HeLa nucleus mesh reconstruction was performed using the bioimage informatics platform Icy (32). Starting from the images with the nuclei and overexpressed lamin skeletons, we applied the Icy HK-Means plugin to obtain 3D nuclear regions of interest for each temporal acquisition. This segmentation method uses, in fact, a K-Means classification to detect clustered objects corresponding, in our case, to the nucleus structures. The final 3D meshes of the outer nuclear membrane have been obtained thanks to the Icy Active Contours plugin (36). The parameters used for the reconstruction are the default ones except for the values of contour smoothness, contour sampling, and region sensitivity. For these three parameters, we used, respectively, the values in the ranges 0.028–0.032, 1.9–2.1, and 2–3.

Local displacements

The total volume change $\Delta\mathrm{Vol} = \mathrm{Vol}(M_1) - \mathrm{Vol}(M_0)$ between two meshes M_0, M_1 of a given cell at different time points is a global measure that gives only summarized information on morphological changes. Although $\Delta\mathrm{Vol}$ can reveal key information in some situations, most local morphological changes like [XX, YY, and ZZ (blebs, etc.)] can take place at fixed volume, remaining blind to $\Delta\mathrm{Vol}$. To circumvent this issue and detect local morphological changes, we develop the concept of local displacements d_j, which can be interpreted as the distance each face of M_0 should move to turn M_0 into M_1.

Alternatively, one can think of local displacements as a decomposition of the total volume change,

$$\sum_j d_j s_j \simeq \Delta\mathrm{Vol}, \tag{3}$$

where s_j denotes the surface areas of the faces of M_0.

Computation of local displacements

We estimate local displacement d_j of a triangular face j of mesh M_0 with respect to mesh M_1 by averaging the projection of the displacement vectors $\vec{q}_i$ onto the face normal $\vec{n}_j$. The average is taken over the vertices i that form face j. Displacement vectors $\vec{q}_i$ are defined as $\vec{q}_i = \mu(\vec{v}_i) - \vec{v}_i$, where μ is the optimal matching between M_0 and M_1. The optimal matching μ is found by minimizing the sum of distances between pairs of matched vertices, $\mu = \mathrm{argmin}_m \sum \|m(v_i) - v_i\|$, over all possible one-to-one matchings m between the ^{i}vertices of M_0 and M_1.

In summary, the local displacements of a mesh M_0 with respect to a mesh M_1 are computed as follows:

1) Find the matching μ that minimizes the total distance:

$$\mu = \mathrm{argmin}_m \sum_i \|m(v_i) - v_i\|, \tag{4}$$

where $m: v_0 \rightarrow v_1$ is a one-to-one correspondence between the vertices of M_0 and those of M_1. If $|v_0| \neq |v_1|$, we resort to subsampling the mesh with the largest number of vertices. We solve Eq. 4 using the Hungarian algorithm (37) as implemented by the *scipy.optimize.linear_sum_assignment* function from the SciPy library (35).

2) Compute the displacement vectors $\vec{q}_i$ of each vertex:

$$\vec{q}_i = \mu(v_i) - v_i$$

3) Compute the normal vectors to all faces $\vec{n}_j$.
4) Compute the projections of q_i on n_j.
5) The local displacement d_j is the average of $q_i \times n_j$ over the vertices i that form face j:

$$d_j = \vec{n}_j \cdot \left(\frac{1}{3} \sum_{i=0}^{2} \vec{q}_i \right) \tag{5}$$

Local displacement fluctuations

The quantity $\sigma(d)$ reported in Fig. 4 is the standard deviation of the local displacements d_j of each cell.

$$\sigma(d) = \sqrt{\frac{1}{N} \sum_j d_j^2 - \left(\frac{1}{N} \sum_j d_j \right)^2} \tag{6}$$

Large values of $\sigma(d)$ are associated with heterogenous morphological, whereas low values of $\sigma(d)$ are obtained when the changes are homogeneous over the nucleus surface. In particular, volume changes due to a uniform shrinking or expansion would entail a value of $\sigma(d) \ll 1$.

Statistical significance tests

The *p*-values reported in Fig. 1 and Figs. S7, *C* and *F*, and S8, *A*, *B*, and *D* are obtained via a Kolmogorov-Smirnov test comparing the distribution of the relevant magnitude among the two groups (Doxy versus No Doxy or Healthy

versus HGPS). The computation is implemented via the "ks_2samp" function from SciPy library (35). The *p*-values reported in Figs. S7, *B* and *E*, and S8 *C* are instead computed using a *t*-test for independent samples with unequal sample sizes and unequal variances, implemented through the "ttest_ind" function from SciPy library (35). We use the Kolmogorov-Smirnov test to assess the statistical significance of differences in local displacements when comparing treated versus untreated cells. In Fig. 4, *p*-values below 0.05 are marked with *, and *p*-values below 0.01 are marked with **. For each time step, we correct *p*-values for multiple testing using the Holm-Sidak method as implemented in the "statsmodel.stats.multites" python library. We also used *t*-test when indicated.

Computational modeling

We consider a discretized model for the cell nucleus composed by a flexible coarse-grained shell representing nuclear envelope and lamina, coupled to a set of coarse-grained polymers representing chromatin and also to a set of randomly distributed points representing cytoskeletal elements. At this level of coarse graining, the intention is to capture the mechanical properties of the essential nuclear components without resorting to detailed modeling of their structure. A sketch of the model is reported in Fig. S1, and the list of parameters is summarized in Table S2.

Chromatin

Chromatin is modeled in analogy with previous coarse-grained simulation studies (26,27,38,39). We consider a set of 46 polymers with 128 monomers each. Monomers are coupled by harmonic springs with spring constant 10^{-3} N/m (26,27) and a harmonic angular coupling with equilibrium angle $130°$ and spring constant 2×10^{-16} J · rad^{-2}. To avoid chromatin overlaps, monomers also interact with a truncated Lennard-Jones interaction with $\varepsilon = 10^{-3}$ pJ, $\sigma = 0.12$ μm, and a cutoff of 0.2 μm, which provide an effective short-range repulsion. Chromatin polymers are initialized as nonoverlapping random walks, each centered on a random site within the spherical nucleus. This initial condition ensures the presence of chromatin segregation into separated territories, as suggested by experiments (40). The initial chromatin configuration is first relaxed using an NVE integrator with particle step size limited to 1 nm per time step of 10^{-9} s for 5×10^4 time steps. The system is then brought to thermal equilibrium using an NVE integrator with Langevin thermostat with target temperature 300 K and damping $\gamma = 10^6$ s^{-1}, with a time step of 10^{-7} μs, for 5×10^7 steps before the nuclear envelope and cytoskeleton are added to the simulation.

Nuclear envelope

The nuclear envelope is modeled as a triangulated sphere, using 10,242 nodes in the triangulation, and each node is treated as a particle in a molecular dynamics simulation. The energy cost of stretching the shell is implemented by coupling each node of the triangulation by linear springs to its neighbors with spring constant 5×10^{-3} N m^{-1} (22) for all bonds. Bending the shell also has an energy cost, which is implemented by coupling each triangular plaquette of the sphere to its neighbors using a harmonic coupling in the angle between two plaquettes, with equilibrium angle $180°$. We use a spring constant for this coupling of 10^{-15} J rad^{-2} inside the domains and 10^{-17} J rad^{-2} on the domain walls. This is larger than the literature value of 10^{-19} J rad^{-2} (22), but
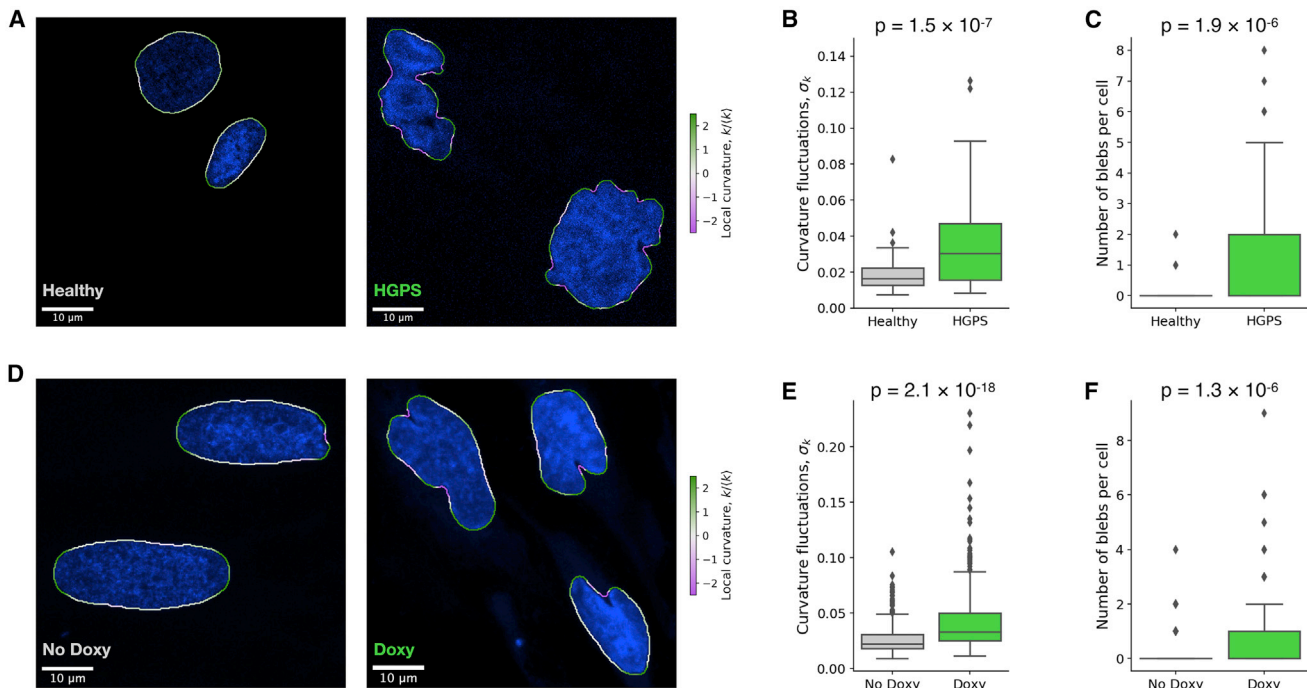
FIGURE 1 Progerin expression affects nuclear morphology. Typical nuclei obtained from (*A*) subconfluent HGPS cells (HGPS), healthy mother of HGPS patient (Healthy), or (*D*) HeLa Tet-On progerin-expressing cells without Doxy treatment (No Doxy) or after induction with 10 ng/mL with doxycyclin (Doxy) are shown. Subconfluent cells were fixed with ice-cold methanol, then incubated with anti-PanLamin (1:50, ab20740; Abcam) at 4°C overnight and with AlexaFluo488 (1:250, ab15113; Abcam) for 1 h at RT. Nuclei were stained with DAPI. Images were acquired with a Leica SP2 laser scanning confocal microscope. Quantification of morphological alterations of (*B* and *C*) HGPS cells and mother of HGPS cells and (*E* and *F*) HeLa Tet-On progerin-expressing cells (Doxy) and HeLa Tet-On cells without Doxy treatment (No Doxy) by computing the number of blebs (*B* and *E*) and the curvature fluctuations (*C* and *F*) as described in the Materials and Methods. Statistics was performed over 297 No Doxy nuclei, 330 Doxy nuclei, 87 healthy nuclei, and 87 HGPS nuclei. The *p*-values reported were obtained via a Kolmogorov-Smirnov test comparing the distribution of the relevant magnitude among the two groups (Healthy versus HGPS or Doxy versus No Doxy). The computation is implemented via the "ks_2samp" function from the SciPy library (35). Data have been collected over at least three independent experiments. Error bars in boxplots indicate minimum and maximum quartiles, boxes are first and third quartiles. To see this figure in color, go online.

we find this is necessary to prevent crumpling of the shell. The nuclear envelope is initialized as a sphere of radius 6 μm. To prevent chromatin polymers from passing through the shell, the chromatin and shell particles interact with a truncated Lennard-Jones interaction with $\varepsilon = 10^{-3}$ pJ, $\sigma = 0.6\,\mu$m, and a cutoff radius of $r_c = 0.6\,\mu$m. When the nuclear envelope is created, monomers in the relaxed chromatin configuration that are within distance 0.35 μm of the nuclear envelope are able to couple to the nuclear envelope with probability p_0, which we can fine tune to obtain a given lamin-chromatin link density p, defined as the average number of links per node of the triangulated shell.

Lamin domains

A key feature of our model is the presence of spatial domains in the lamina, which are bounded by "domain walls" that are easier to bend than the domains. The existence of spatial domains was demonstrated experimentally in (10), and we hypothesize that the domain walls are more bendable than the domains themselves. The nodes are assigned to domains by generating a domain pattern on the surface of the sphere by placing 10 domain centers uniformly at random and then generating the domain walls using Voronoi tessellation. When the nuclear envelope is created, monomers in the relaxed chromatin configuration that are within distance 0.35 μm of the nuclear envelope are able to couple to the nuclear envelope only if the envelope particle is on a domain wall. In all cases, coupling is implemented via harmonic springs with stiffness $k_{tether} = 10^{-2}$ N/m.

Coupling to the cytoskeleton

The nuclear envelope is also coupled to a set of 100 randomly placed points representing elements of the cytoskeleton. The coupling is implemented via linear springs that connect randomly selected points on the lamina, with spring constant k_{cyto}, which we vary in the range 10^{-3}–10^{-2} N m^{-1}. To simulate cytoskeletal activity, each cytoskeletal element follows an oscillatory motion $\vec{R}_i = \vec{R}_i^0 - \vec{A}_i \cos(\omega_i t)$ with frequencies randomly distributed in the range $[0.05, 0.2]$ μs^{-1} and amplitudes also randomly distributed in the range $[-1, 1]\mu$m.

Simulation details

The system is first relaxed using an NVE integrator with particle step size limited to 1 nm per time step of 10^{-9} s for 10^6 time steps. The system is then brought to thermal equilibrium using an NVE integrator with Langevin thermostat with target temperature 300 K and damping constant $\gamma = 10^4$ μs^{-1}, with a time step of 10^{-6} μs, for 6×10^7 steps. All simulations are implemented in LAMMPS (41).

RESULTS AND DISCUSSION

Progerin induction in HeLa cells modifies nuclear morphology and chromatin organization

The Tet-On system is based on reverse tetracyclin activation. Here, we used the Tet-On 3G system, which is 100-fold more sensitive and sevenfold more active than the original Tet-On (see Materials and Methods for technical information). In our cellular model, the level of expression of progerin is induced by Doxy. As shown in Fig. S2, 10 ng/mL Doxy is the minimal concentration that is able to induce progerin expression. To check the specificity of the induction of progerin after the treatment with Doxy, we used two internal controls according to the manufacturer's instructions: we compared the cells treated with Doxy with respect to cells not exposed to Doxy (No Doxy). The second control was to investigate the level of expression of progerin in cells transfected with an empty vector, untreated or after treatment with Doxy (Fig. S2 C). In all these control experiments, we

did not observe any progerin induction. For completeness in Fig. S3, we show the mCherry expression and PanLamin for the same conditions as in Fig. S2 and, in Fig. S4, an example of HeLa cells expressing mEmerald and WT lamin A or pEGFP-Δ50 lamin A 48 h after transfection. We also quantified by Western blot the level of expression of lamin A and B under the induction of progerin without finding any significant changes due to the presence of progerin (Fig. S5).

It was reported in the literature that in cells from HGPS patients, the ratio between the amount of progerin/lamin A proteins is between 0.5 and 2 (10,42,43). This variability is possibly due to the specificity of each patient. Here, we quantified the ratio between progerin/lamin A proteins in HeLa Tet-On progerin-expressing cells and found a value around 1.5–2, as shown in Fig. S6.

To confirm that our cellular model faithfully represents the morphology of HGPS nuclei, we compared the number of blebs and the curvature fluctuations observed in HeLa Tet-On progerin-expressing cells (Doxy) with those observed in control cells (No Doxy) and performed a similar analysis for fibroblasts obtained from an HGPS patient (HGPS) and his healthy mother (Healthy) (Fig. 1). Using the same samples, we also measured a blebbing index, defined as the average curvature restricted to the region of negative curvature (see Materials and Methods for more details) and the number of cells with blebs (see Fig. S7). All these different quantitative measurements confirmed that nuclei in both HeLa Tet-On progerin-expressing cells and HGPS cells display highly significant alterations with respect to their controls, confirming the capability of our model to faithfully recapitulate the main features of the nuclei from HGPS patients. As a further control, we report in Fig. S8 morphological measurements in cells transfected with an empty vector. In this case, treatment with Doxy does not induce any morphological alteration.

Finally, it is known that HGPS patients show important differences in higher-order chromatin organization such as specific changes in chromatin-modifying enzymes (i.e., heterochromatin protein 1, HP1) (44,45). Consistently, we found an increased expression of HP1 in HeLa Tet-On progerin-expressing cells (Fig. S9).

Progerin induction affects the coupling between the cytoskeleton and the nuclear shell

Because the interaction between fascin and giant nesprin or nesprin-2 requires the phosphorylation of fascin at serine 39 (S39), we investigated the possible impairment of the fascin/nesprin-2 complex in HeLa Tet-On progerin-expressing cells. As shown in Fig. S10, nesprin-2 associates with the outer nuclear membrane, exposing its N-terminal domain to the cytoplasm, where it binds cytoskeletal actin through fascin, and its C-terminal domain to the perinuclear space, where it binds to SUN1/2 and emerin. According to (21), fascin can interact properly with nesprin-2 only when it is phosphorylated (S39). First, we checked the level of expression of giant
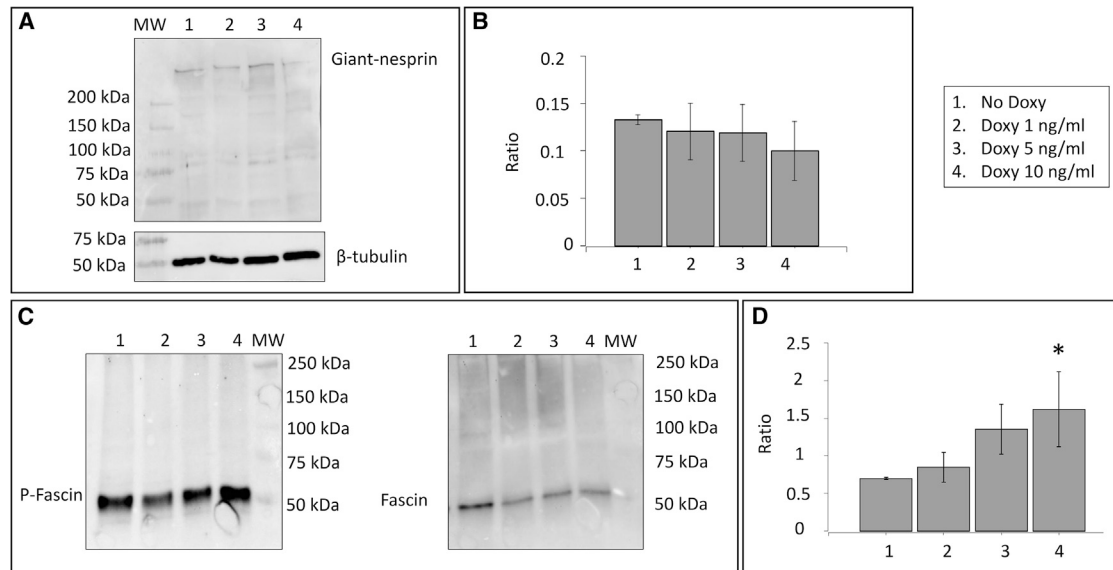
FIGURE 2   Progerin induction leads to fascin phosphorylation in S39 without affecting nesprin-2 expression. (*A*) Typical experiment of Western blot of giant nesprin in HeLa Tet-On 3G progerin-expressing cells treated with increasing concentration of Doxy or without (No Doxy) is shown. 20 μg total protein was loaded on 10% polyacrylamide gel, transferred on PVDF, and incubated with nesprin-2 (1:1000, MABC86; Merck Millipore) overnight at 4°C. Anti-β-tubulin antibody (1:5000, T8328; Sigma-Aldrich) for 1 h at RT was used as housekeeping. (*B*) Densitometric analysis of two independent Western blot experiments of giant nesprin Western blot as shown in (*A*) is given. Densitometric analysis was carried out with ImageJ software. The *y* axis shows the ratio between the mean of the densitometric value of giant nesprin with respect to the housekeeping β-tubulin. Statistical significance was established by *t*-test. (*C*) Typical Western blot of S39-fascin in fascin-immunoprecipitated samples obtained from HeLa Tet-On progerin-expressing cells treated or untreated with Doxy is shown. Subconfluent cells were processed for immunoprecipitation as described in the Materials and Methods. Briefly, 500 μg of total proteins was incubated with anti-fascin antibody (1:100, ab126772; AbCam) overnight at 4°C under stirring. 50% bead slurry of Protein A-Agarose (P9269; Sigma-Aldrich) was added to the lysate and reincubated with gentle rocking for 2 h at 4°C. After three washes with 500 μL of lysis buffer, the sample was resuspended in 30 μL 2× Laemmli sample buffer and heated to 90°C for 5 min, and 15 μL of immunoprecipitated sample was loaded on 10% SDS-PAGE for Western blot. (*D*) Densitometric analysis of two independent experiments as shown in (*C*) is given. The *y* axis shows the ratio between the mean of the densitometric value of S39-fascin and fascin.

nesprin in HeLa Tet-On progerin-expressing cells with respect to cells not induced by Doxy. As shown in Fig. 2, the induction of progerin did not change the level of expression of nesprin-2. On the other hand, we observed an increase in the expression level of S39-fascin as progerin's level of expression increases (Fig. 2). Hence, our observation suggests that the expression of progerin enhances the coupling between the cytoskeleton and the nuclear shell (Fig. 2; Fig. S10).

Progerin induction affects chromatin-lamin tethers

To study the role of progerin induction in the tethering between lamins and chromatin, we investigated the presence and the interaction between SUN1 or emerin with all lamins using the PanLamin antibody in HeLa Tet-On progerin-expressing cells. Fig. S11 shows that neither SUN1 nor emerin's level of expression changes significantly in dependence on the expression of progerin. We then investigated the dependence on progerin expression of the interaction between lamins and SUN1 or emerin using the proximity ligation assay. In Fig. 3, we show a typical experiment and its quantification by counting the number of the spots, each representing an interaction between SUN1 or emerin and lam-

ins, as detected with the PanLamin antibody. Fig. 3 shows a significant reduction in the coupling between emerin and lamins upon progerin induction. In contrast, the coupling between SUN1 and lamins is unaffected by progerin induction Fig. 3.

Progerin induction slows down collective cell migration

To assess the effect of progerin induction on functional properties of the cell, we performed wound-healing assays. As shown in Fig. S12 *A*, the velocity distributions appear altered by progerin induction, leading to a slower collective migration. Although the effect is small, it is statistically significant according to the Kolmogorov-Smirnov test. Accordingly, the front position of progerin-induced cells advances more slowly than in control cells (see Fig. S12 *B*).

Nuclear surface fluctuations driven by cytoskeletal activity are affected by progerin

Forces generated by the cytoskeleton can affect chromatin through the links with the nuclear envelope and the lamina, as illustrated in Fig. S10. To quantify the effect of
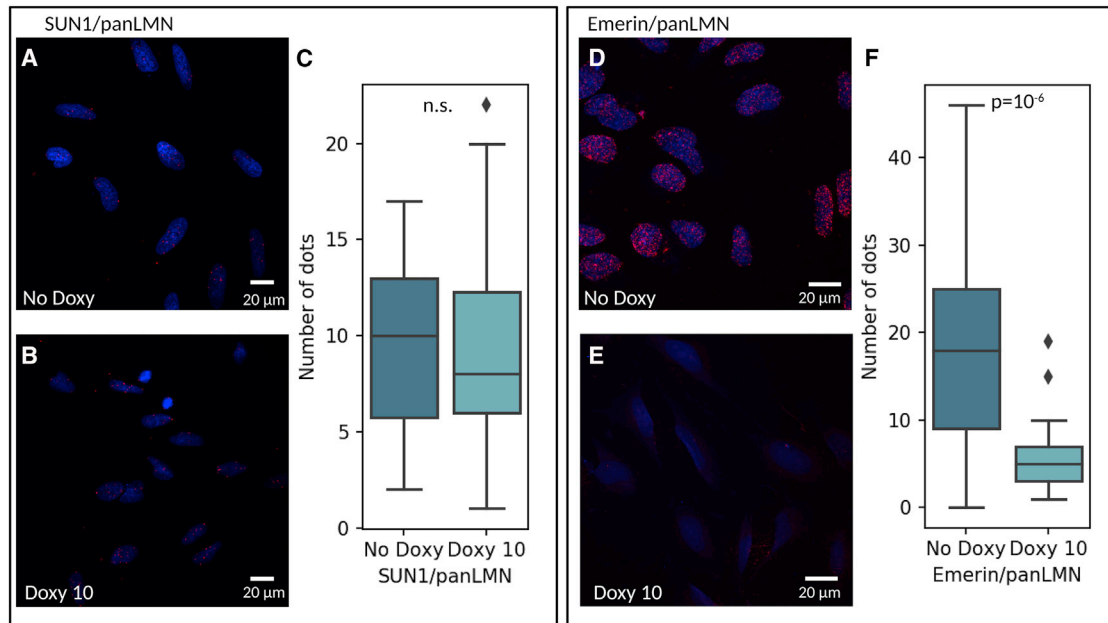
FIGURE 3 Effect of progerin induction on nuclear tethering factors by proximity ligation assay. The tethering is quantified by the proximity ligation assay measuring the interaction between all lamins detected using PanLamin antibody and (A and B) SUN1 or (D and E) emerin. Briefly, subconfluent cells were fixed on slides with ice-cold 100% methanol for 5 min. Slides were then incubated in a humidity chamber overnight at 4°C with PanLamin (1:50, ab20740; Abcam) antibody and with SUN1 (1:200, ab103021; Abcam) or emerin (1:200, ab40688; Abcam). After washing, the samples were incubated in a preheated humidity chamber for 1 h at 37°C with anti-rabbit PLUS and anti-mouse MINUS PLA probes diluted 1:5. Ligation and amplification steps were performed according to the manufacturer's instructions. Slides were mounted with Duolink In Situ Medium. The number of aggregates linking (C) SUN1 or (F) emerin and lamins are quantified as described in the Materials and Methods. The analysis has been carried out on 72 nuclei for SUN1 (36 without Doxy and 36 with Doxy) and 76 nuclei for emerin (53 without Doxy and 23 with Doxy). Statistical significance is established by the Kolmogorov-Smirnov method. Data have been collected over at least three independent experiments. Error bars in boxplots indicate minumum and maximum quartiles, boxes are first and third quartiles. To see this figure in color, go online.

cytoskeletal activity on the nuclear envelope when progerin is expressed, we studied time-dependent shape fluctuations in HeLa cells transiently transfected with GFP—Δ50 lamin A and mEMERALD-lamin A WT. To this end, we exposed the cells to agents that are able to stabilize actin (jasplakinolide), depolymerize actin (cytochalasin D), affects myosin activity (blebbistatin), or inhibit the nucleation of actin polymerization (SMIFH2), and then we wash out the drug and start to acquire images with a confocal microscope (5). We thus reconstructed the 3D mesh of nuclear surfaces according to Materials and Methods, and from each time series of nuclear meshes, we computed the local displacement fields d_i, indicating how much each node of the mesh has been displaced from the beginning (see Fig. 4 A). Finally, to quantify the fluctuations of the mesh in each instance, we computed the standard deviation of d_i as a function of time. As shown in Fig. 4 B, progerin overexpression leads to significantly larger time-dependent fluctuations in the nuclear envelope. Notice that larger fluctuations are not trivially related to the presence of blebs. Fluctuations here are defined relative to a reference frame, so a blebbed surface not changing in time would yield no fluctuations. Moreover, the treatments with blebbistatin (Fig. 4, C and D) and SMIFH2 (Fig. 4, I and J) and, to a lesser extent, with jasplakinolide (Fig. 4, G and H) showed significant differences in

the presence of progerin. The general conclusion is that hindering cytoskeletal activity affects progerin-expressing cells, reducing their nuclear surface fluctuations.

Progerin affects the interaction between lamins and polycomb proteins

Polycomb group (PcG) proteins play an important role in chromatin remodeling during development. High-throughput data combined with microscopy analysis revealed a specific organization of their targets in chromatin loops (46,47) that is altered in lamin A null cells (47). To investigate the interactions between PcG proteins and lamins, we carried out a proximity ligation assay. According to this technique, a fluorescent signal is detectable when two proteins are in close proximity (less than 40 nm). First, we checked which PcGs were expressed in Tet-On HeLa cells without the Doxy treatment and after the induction of progerin. As shown in Fig. S13, we detected the presence of EZH2, SUZ12, Ring1A, and BMI1. In contrast, Ring1B was not expressed in a detectable way. We carried out a proximity ligation assay for the two PcGs belonging to the two PcG machineries BMI1 (PcG1) and SUZ12 (PcG2), which are involved in chromatin remodeling through two distinct mechanisms (48), with all the lamins using the
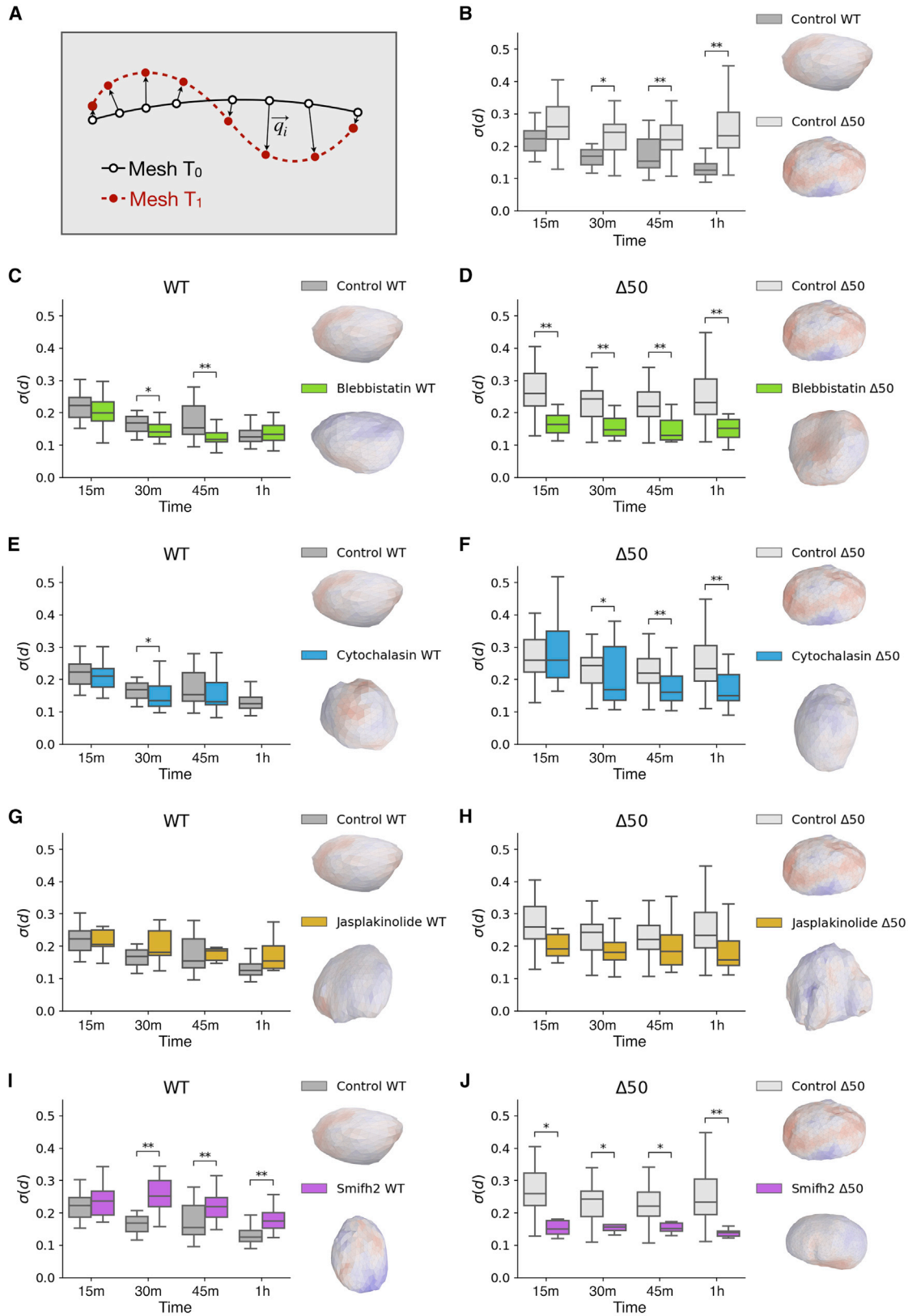
FIGURE 4 Progerin induction leads to larger shape fluctuations due to cytoskeletal activity. (*A*) Illustration of local displacements method is shown: given meshes for two time points T_0, T_1, the algorithm finds the vectors v_i used to compute $\sigma(d)$; see Materials and Methods for details. (*B*) Boxplot of $\sigma(d)$ over time for untreated cells is shown, comparing cells overexpressing WT lamin A (*dark gray*) or $\Delta50$ lamin A (*light gray*). (*C*) and (*D*) show boxplots of $\sigma(d)$ over

(legend continued on next page)
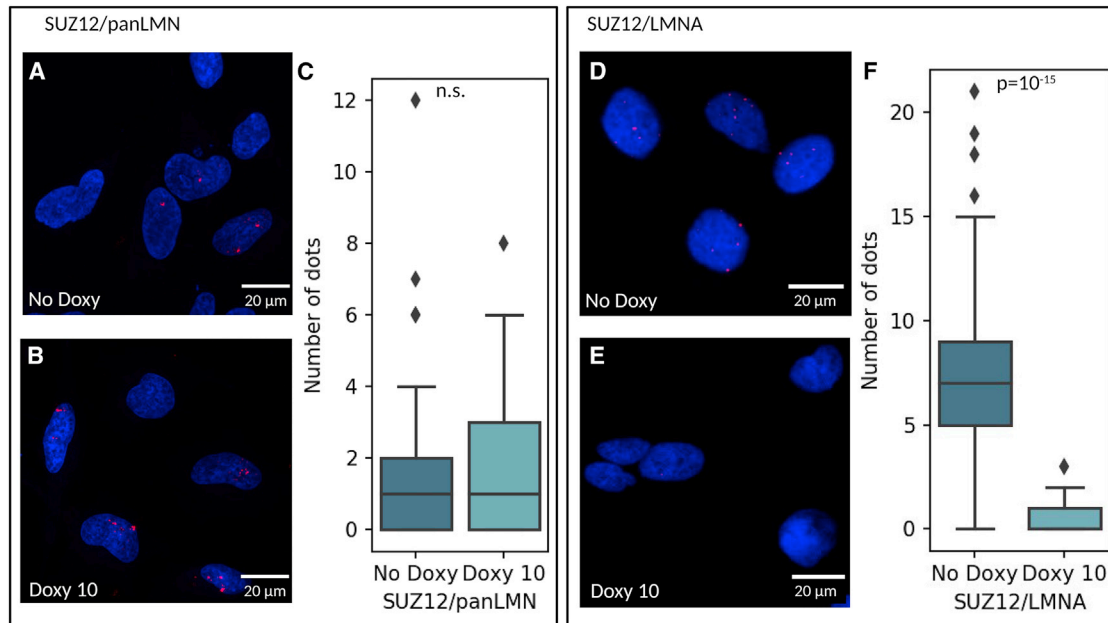
FIGURE 5 Effect of progerin induction on the interaction of polycomb protein SUZ12 and lamins by proximity ligation assay. The tethering is quantified by the proximity ligation assay measuring the interaction between (*A* and *B*) all lamins (panLMN) or (*D* and *E*) lamin A and PcG SUZ12. Briefly, subconfluent cells were fixed on slides with ice-cold 100% methanol for 5 min. Slides were then incubated in a humidity chamber overnight at 4°C with PanLamin (1:50, ab207404; Abcam) or anti-lamin (1:100, ab8980; Abcam) antibody with SUZ12 (1:800, mAb 3737; Cell Signaling). After washing, samples were incubated in a preheated humidity chamber for 1 h at 37°C with anti-rabbit PLUS and anti-mouse MINUS PLA probes diluted 1:5. Ligation and amplification steps were performed according to manufacturer's instructions. Slides were mounted with Duolink In Situ Medium. (*A*), (*B*), (*D*), and (*E*) show typical experiments for each experimental condition. The number of aggregates linking SUZ12 and lamins (*C* for PanLamin and *F* for lamin A) are quantified as described in the Materials and Methods. The analysis was carried out on 79 nuclei for PanLamin (33 without Doxy and 46 with Doxy) and 81 for lamin A (41 without Doxy and 40 with Doxy). Statistical significance is established by the Kolmogorov-Smirnov method. Data have been collected over at least three independent experiments. Error bars in boxplots indicate minimum and maximum quartiles, boxes are first and third quartiles. To see this figure in color, go online.

PanLamin antibody or with lamin A. As shown in Fig. 5, the interaction between SUZ12 and lamin A is significantly changed by the induction of progerin, whereas no effect is revealed for BMI1 (Fig. S14).

Computational model indicates the relevance of tethering on lamin domains walls for nuclear bleb formation

To further investigate the role of chromatin/lamin tethering for nuclear morphological alteration, we performed numerical simulations according to the protocol discussed in the modeling section. We first considered the case in which chromatin tethers were distributed uniformly on the nuclear envelope. As shown in Fig. 6, *A–C*, although surface deformations are present, no distinct blebs are observed. We then varied two key parameters: the density of tethers ρ and their stiffness k_{tether}. As illustrated in Fig. S15, increasing the tether stiffness and their density leads to nuclear alterations.

Yet, these morphological alterations are in the form of creases and crumples that look qualitatively very different from blebs observed experimentally.

Previous experimental results indicate that in HGPS nuclei, lamin is organized into domains characterized by distinct orientations, as revealed by polarized light microscopy (10). In WT nuclei, lamin filaments have no preferred orientation, whereas in HGPS nuclei, lamin filaments are ordered within distinct domains. To take this observation into account, we introduced lamin domains in the model by defining domain boundaries with low bending stiffness so that the nuclear shell folds more easily along those regions. Even in this case, blebs were not observed (Fig. 6, *D* and *E*), and we recorded only minor alterations with respect to a similar configuration without domain boundaries (Fig. 6, *A–C*).

We then investigated the effect of lamin domains on the coupling between lamins and chromatin. Modifications of the coupling is suggested by the experiments reported in

time, comparing control cells (*gray*) with blebbistatin-treated cells (*green*) for (*C*) WT lamin A and (*D*) progerin cases. Additional panels show cells treated with (*E* and *F*) cytochalasin (*blue boxplots*), (*G* and *H*) jasplakinolide (*orange boxplots*), and (*I* and *J*) SMIFH2 (*violet boxplots*). For each time point, local displacements are computed with respect to the previous time point. Statistical significance is measured with Kolmogorov-Smirnov tests, with ** (*) marking $p < 0.01\ (0.05)$. *p*-Values are corrected for multiple testing; see Materials and Methods for details. Data have been collected over at least three independent experiments. Error bars in boxplots indicate minimum and maximum quartiles, boxes are first and third quartiles. To see this figure in color, go online.
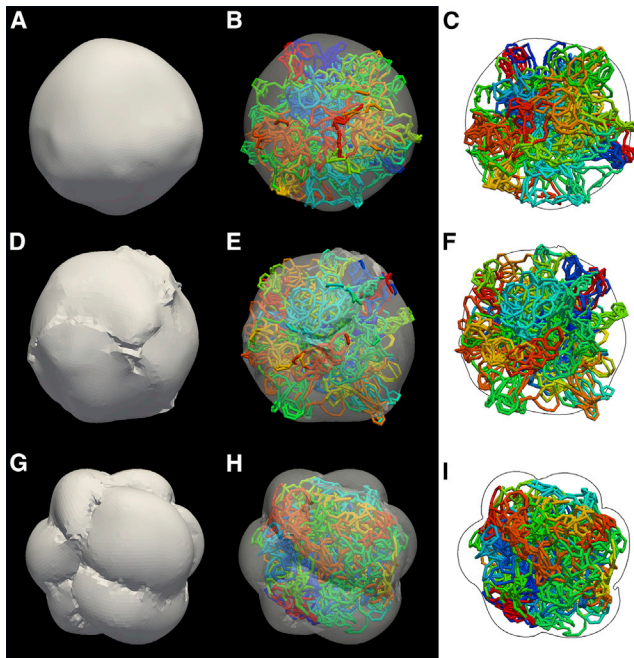
FIGURE 6 Formation of nuclear blebs is induced by a strong chromatin tethers localized on lamin domain boundaries. (A–C) Simulations without lamin domains and uniform distribution of lamin-chromatin tether are shown. (D–F) Simulations with lamin domains and uniform distribution of lamin-chromatin tether are shown. (G–I) Simulations with lamin domains and lamin-chromatin tethers localized along the domain boundaries are shown. Only in the last case do we observe the formation of blebs. In all cases, the link density is $p = 0.4$. To see this figure in color, go online.

FIGURE 7 Nuclear shape fluctuations depend on cytoskeletal tethering stiffness. Simulations of shape fluctuations induced by cytoskeletal contraction for different values of the stiffness of the tether k_{cyto} are shown. (A) $k_{cyto} = 10^{-3}$ N/m, (B) $k_{cyto} = 5 \times 10^{-3}$ N/m, and (C) $k_{cyto} = 10^{-2}$ N/m. (D) The standard deviation of the radial displacements is shown as a function of k_{cyto}. All the comparisons are statistically significant ($p < 10^{-10}$ according to the Kolmogorov-Smirnov test). Errror bars in the boxplot indicate minimum and maximum quartiles, boxes are first and third quartiles. To see this figure in color, go online.

Fig. 3, *D–F*, showing a net reduction of the interactions between lamin and emerin, a chromatin tethering factor. To incorporate this observation into the model, we notice that lamins are disordered in WT nuclei, whereas they are ordered within domains in HGPS nuclei. Hence, it is reasonable to assume that chromatin-lamin coupling occurs at the domain wall boundaries where lamin organization is less ordered. Indeed, when chromatin tethers were attached exclusively at the lamin domain boundaries, we were able to recover nuclear shapes with blebs similar to those encountered in experiments (Fig. 6, *F–H*).

To confirm that tethering to the lamin domain is essential to account for blebs, we considered alternative nonuniform distribution of the chromatin-lamin tethers. For instance, in Fig. S16 *A*, we report simulations results obtained placing all the tethers in a single octant of the envelope. No blebs were found, but only localized depressions. When tethers are instead placed along a single line, the sphere was found to crumple in a way that is very different from the experimental images (Fig. S16 *B*). The model also allowed us to describe the role of the elasticity of the nuclear envelope. In particular, we find that when the bending stiffness is reduced, the smooth blebs observed in Fig. 6 *G* give way to the crumpled surface shown in Fig. S17. Finally, we studied the effect of the stiffness of the chromatin tether on the

bleb morphology and found that by reducing the stiffness, blebs were less pronounced (Fig. S18). In sum, our computational results show that the local organization of the chromatin-lamin tethers is the key factor controlling bleb formation. In particular, lamin domain wall boundaries are pulled inside the nucleus by chromatin tethers, creating the folds required for bleb formation.

Computational model confirms the role of cytoskeleton in nuclear shape fluctuations

As discussed in the previous section, the computational model is able to reproduce the morphological alterations of HGPS nuclei by considering the combined effects of lamin domains and chromatin-lamin tethers. We thus decided to use the model to better understand why nuclear shape fluctuations are enhanced when progerin is overexpressed (see Fig. 4 *B*). We reported in Fig. 2 *D* that progerin induction leads to increased fascin phosphorylation, leading to more stable couplings between the cytoskeleton and lamins. We thus incorporated this information into the model by varying the strength of the coupling between cytoskeleton and the nuclear shell.

We simulated cytoskeletal contractions by a set of randomly placed oscillating points attached to the nuclear lamina by springs of stiffness k_{cyto}, as described in the model section. Increased fascin phosphorylation was represented by an increasing value of k_{cyto}. We then studied

the fluctuations of the nuclear shape induced by cytoskeletal activities (for an illustration of the fluctuations, see Fig. 7 A; Video S1). To quantify nuclear fluctuations, we computed the standard deviation $\sigma(d)$ of the radial projection of the local displacement fields as a function of k_{cyto}, in close analogy with the 3D morphological analysis summarized in Fig. 4. The results reported in Fig. 7 B show that stronger cytoskeletal coupling leads to enhanced fluctuations in good agreement with the results reported in Fig. 4 B, indicating that progerin overexpression is associated with larger nuclear fluctuations.

CONCLUSIONS

In this work, we introduced an inducible cellular model for progerin, the mutated form of lamin A responsible for HGPS. Through this cellular model, we analyzed how progerin affects nuclear tethering with chromatin and the cytoskeleton. Our results show that progerin expression leads to enhanced tethering between the cytoskeleton and the nuclear shell through the phosphorylation of S39-fascin and, at the same time, to a reduced interaction between lamins and emerin, a known chromatin tether. These changes are reflected in alterations of the mechanical response of the nucleus. In particular, cytoskeletal-induced surface fluctuations of the nuclear shell are increased upon progerin expression.

It has been shown that the coupling between the cytoskeleton and the nuclear shell can affect gene regulation (49) by polycomb-mediated chromatin remodeling (50). Hence, we studied the interaction between lamins and polycomb proteins upon progerin induction. Our findings show that progerin induction reduces the interactions between lamins and the polycomb protein SUZ12, suggesting progerin expression might impact PRCs-mediated gene expression regulation.

Finally, we proposed a computational model for nuclear mechanics in which we simulate the conditions leading to nuclear morphological alterations, focusing in particular on the blebs observed in HGPS. Our results show that the presence of lamin domains is essential to recapitulate in silico the observed morphology. A crucial role in bleb formation is played by chromatin-lamin tethers: the presence of homogeneously distributed tethers suppresses blebs or leads to wrinkling of the surface. Blebs are only observed when tethering is concentrated at the boundaries of lamin domains.

Our results are not obtained directly from HGPS cells but from an induced cellular model of progerin in HeLa cells that, however, recapitulates the main features of nuclear morphology and chromatin organization of HGPS cells, as shown, for instance, by the expression of HP1. Our cellular model overcomes many practical experimental limitations posed by the study of HGPS cells that are able to grow in vitro only for a few passages.

All in all, our study highlights that progerin induction affects, in crucial ways, the tethering between cytoskeleton, lamins, and epigenetic regulation of chromatin status. Simulations suggests that the strength and geometrical organization of these tethers appear to control the morphological alteration observed in the nuclei of HGPS cells. Our observations could be relevant for HGPS, for which therapeutic strategies should aim at restoring the cytoskeleton-lamin-chromatin coupling integrity.

SUPPORTING MATERIAL

AUTHOR CONTRIBUTIONS

M.C.L. performed experiments. M.R.F., F.F.-C., G.C., O.C., and S.Z. analyzed data. Z.B. and S.Z. designed the computational model. Z.B. and S.B. performed numerical simulations. C.A.M.L.P. designed and coordinated the study. S.Z. and C.A.M.L.P. wrote the manuscript.

ACKNOWLEDGMENTS

REFERENCES

1. Lammerding, J., P. C. Schulze, …, R. T. Lee. 2004. Lamin A/C deficiency causes defective nuclear mechanics and mechanotransduction. *J. Clin. Invest.* 113:370–378.

2. Lammerding, J., L. G. Fong, …, R. T. Lee. 2006. Lamins A and C but not lamin B1 regulate nuclear mechanics. *J. Biol. Chem.* 281:25768–25780.

3. Swift, J., I. L. Ivanovska, …, D. E. Discher. 2013. Nuclear lamin-A scales with tissue stiffness and enhances matrix-directed differentiation. *Science.* 341:1240104.

4. Schreiner, S. M., P. K. Koo, …, M. C. King. 2015. The tethering of chromatin to the nuclear envelope supports nuclear mechanics. *Nat. Commun.* 6:7159.

5. Makhija, E., D. S. Jokhun, and G. V. Shivashankar. 2016. Nuclear deformability and telomere dynamics are regulated by cell geometric constraints. *Proc. Natl. Acad. Sci. USA.* 113:E32–E40.

6. Chu, F.-Y., S. C. Haley, and A. Zidovska. 2017. On the origin of shape fluctuations of the cell nucleus. *Proc. Natl. Acad. Sci. USA.* 114:10338–10343.

7. Goldman, R. D., D. K. Shumaker, …, F. S. Collins. 2004. Accumulation of mutant lamin A causes progressive changes in nuclear architecture in Hutchinson-Gilford progeria syndrome. *Proc. Natl. Acad. Sci. USA.* 101:8963–8968.

8. Zwerger, M., C. Y. Ho, and J. Lammerding. 2011. Nuclear mechanics in disease. *Annu. Rev. Biomed. Eng.* 13:397–428.

9. Eriksson, M., W. T. Brown, …, F. S. Collins. 2003. Recurrent de novo point mutations in lamin A cause Hutchinson-Gilford progeria syndrome. *Nature.* 423:293–298.

10. Dahl, K. N., P. Scaffidi, …, T. Misteli. 2006. Distinct structural and mechanical properties of the nuclear lamina in Hutchinson-Gilford progeria syndrome. *Proc. Natl. Acad. Sci. USA.* 103:10271–10276.

11. Verstraeten, V. L. R. M., J. Y. Ji, …, J. Lammerding. 2008. Increased mechanosensitivity and nuclear stiffness in Hutchinson-Gilford progeria cells: effects of farnesyltransferase inhibitors. *Aging Cell.* 7:383–393.

12. Booth, E. A., S. T. Spagnol, …, K. N. Dahl. 2015. Nuclear stiffening and chromatin softening with progerin expression leads to an attenuated nuclear response to force. *Soft Matter.* 11:6412–6418.

13. Berk, J. M., K. E. Tifft, and K. L. Wilson. 2013. The nuclear envelope LEM-domain protein emerin. *Nucleus.* 4:298–314.

14. Clements, L., S. Manilal, …, G. E. Morris. 2000. Direct interaction between emerin and lamin A. *Biochem. Biophys. Res. Commun.* 267:709–714.

15. Zhang, Q., C. Bethmann, …, C. M. Shanahan. 2007. Nesprin-1 and -2 are involved in the pathogenesis of Emery Dreifuss muscular dystrophy and are critical for nuclear envelope integrity. *Hum. Mol. Genet.* 16:2816–2833.

16. Li, P., P. Meinke, …, A. A. Noegel. 2014. Contribution of SUN1 mutations to the pathomechanism in muscular dystrophies. *Hum. Mutat.* 35:452–461.

17. Markiewicz, E., R. Venables, …, C. Hutchison. 2002. Increased solubility of lamins and redistribution of lamin C in X-linked Emery-Dreifuss muscular dystrophy fibroblasts. *J. Struct. Biol.* 140:241–253.

18. Vignjevic, D., S. Kojima, …, G. G. Borisy. 2006. Role of fascin in filopodial protrusion. *J. Cell Biol.* 174:863–875.

19. Jayo, A., M. Parsons, and J. C. Adams. 2012. A novel Rho-dependent pathway that drives interaction of fascin-1 with p-Lin-11/Isl-1/Mec-3 kinase (LIMK) 1/2 to promote fascin-1/actin binding and filopodia stability. *BMC Biol.* 10:72.

20. Elkhatib, N., M. B. Neu, …, D. M. Vignjevic. 2014. Fascin plays a role in stress fiber organization and focal adhesion disassembly. *Curr. Biol.* 24:1492–1499.

21. Jayo, A., M. Malboubi, …, M. Parsons. 2016. Fascin regulates nuclear movement and deformation in migrating cells. *Dev. Cell.* 38:371–383.

22. Vaziri, A., and M. R. K. Mofrad. 2007. Mechanics and deformation of the nucleus in micropipette aspiration experiment. *J. Biomech.* 40:2053–2062, Published online November 16, 2006.

23. Funkhouser, C. M., R. Sknepnek, …, M. Olvera de la Cruz. 2013. Mechanical model of blebbing in nuclear lamin meshworks. *Proc. Natl. Acad. Sci. USA.* 110:3248–3253.

24. Wren, N. S., Z. Zhong, …, K. N. Dahl. 2012. Modeling nuclear blebs in a nucleoskeleton of independent filament networks. *Cell. Mol. Bioeng.* 5:73–81.

25. Banigan, E. J., A. D. Stephens, and J. F. Marko. 2017. Mechanics and buckling of biopolymeric shells and cell nuclei. *Biophys. J.* 113:1654–1663.

26. Stephens, A. D., E. J. Banigan, …, J. F. Marko. 2017. Chromatin and lamin A determine two different mechanical response regimes of the cell nucleus. *Mol. Biol. Cell.* 28:1984–1996.

27. Stephens, A. D., E. J. Banigan, and J. F. Marko. 2018. Separate roles for chromatin and lamins in nuclear mechanics. *Nucleus.* 9:119–124.

28. Marko, J. F. 2008. Micromechanical studies of mitotic chromosomes. *Chromosome Res.* 16:469–497.

29. Marti-Renom, M. A., and L. A. Mirny. 2011. Bridging the resolution gap in structural modeling of 3D genome organization. *PLoS Comput. Biol.* 7:e1002125.

30. Dekker, J., M. A. Marti-Renom, and L. A. Mirny. 2013. Exploring the three-dimensional organization of genomes: interpreting chromatin interaction data. *Nat. Rev. Genet.* 14:390–403.

31. Gibcus, J. H., K. Samejima, …, J. Dekker. 2018. A pathway for mitotic chromosome formation. *Science.* 359:eaao6135.

32. de Chaumont, F., S. Dallongeville, …, J.-C. Olivo-Marin. 2012. Icy: an open bioimage informatics platform for extended reproducible research. *Nat. Methods.* 9:690–696.

33. Thielicke, W., and E. Stamhuis. 2014. PIVlab – towards user-friendly, affordable and accurate digital particle image velocimetry in MATLAB. *J. Open Res. Softw.* 2:e30.

34. Chepizhko, O., C. Giampietro, …, C. A. M. La Porta. 2016. Bursts of activity in collective cell migration. *Proc. Natl. Acad. Sci. USA.* 113:11408–11413.

35. Jones, E., T. Oliphant, and P. Peterson. 2001. SciPy: open source scientific tools for Python. http://www.scipy.org.

36. Dufour, A., R. Thibeaux, …, J.-C. Olivo-Marin. 2011. 3-D active meshes: fast discrete deformable models for cell tracking in 3-D time-lapse microscopy. *IEEE Trans. Image Process.* 20:1925–1937.

37. Kuhn, H. W. 2005. The Hungarian method for the assignment problem. *Nav. Res. Logist.* 52:7–21.

38. Naumova, N., M. Imakaev, …, J. Dekker. 2013. Organization of the mitotic chromosome. *Science.* 342:948–953.

39. Ozer, G., A. Luque, and T. Schlick. 2015. The chromatin fiber: multiscale problems and approaches. *Curr. Opin. Struct. Biol.* 31:124–139.

40. Meaburn, K. J., and T. Misteli. 2007. Cell biology: chromosome territories. *Nature.* 445:379–781.

41. Plimpton, S. 1995. Fast parallel algorithms for short-range molecular dynamics. *J. Comput. Phys.* 117:1–19.

42. Reunert, J., R. Wentzell, …, T. Marquardt. 2012. Neonatal progeria: increased ratio of progerin to lamin A leads to progeria of the newborn. *Eur. J. Hum. Genet.* 20:933–937.

43. Vidak, S., N. Kubben, …, R. Foisner. 2015. Proliferation of progeria cells is enhanced by lamina-associated polypeptide 2α (LAP2α) through expression of extracellular matrix proteins. *Genes Dev.* 29:2022–2036.

44. Scaffidi, P., and T. Misteli. 2008. Lamin A-dependent misregulation of adult stem cells associated with accelerated ageing. *Nat. Cell Biol.* 10:452–459.

45. Gabriel, D., D. Roedl, …, K. Djabali. 2015. Sulforaphane enhances progerin clearance in Hutchinson-Gilford progeria fibroblasts. *Aging Cell.* 14:78–91.

46. Cmarko, D., P. J. Verschure, …, S. Fakan. 2003. Polycomb group gene silencing proteins are concentrated in the perichromatin compartment of the mammalian nucleus. *J. Cell Sci.* 116:335–343.

47. Bantignies, F., and G. Cavalli. 2011. Polycomb group proteins: repression in 3D. *Trends Genet.* 27:454–464.

48. Chittock, E. C., S. Latwiel, …, C. W. Müller. 2017. Molecular architecture of polycomb repressive complexes. *Biochem. Soc. Trans.* 45:193–205.

49. Swift, J., and D. E. Discher. 2014. The nuclear lamina is mechanoresponsive to ECM elasticity in mature tissue. *J. Cell Sci.* 127:3005–3015.

50. Le, H. Q., S. Ghatak, …, S. A. Wickström. 2016. Mechanical regulation of transcription controls Polycomb-mediated gene silencing during lineage commitment. *Nat. Cell Biol.* 18:864–875.